

SCIENTIFIC REPORTS

OPEN

Optimizing the Intralayer and Interlayer Compatibility for High-Efficiency Blue Thermally Activated Delayed Fluorescence Diodes

Received: 09 September 2015

Accepted: 18 December 2015

Published: 29 January 2016

Chunbo Duan¹, Chaochao Fan¹, Ying Wei^{1,2}, Fuquan Han¹, Wei Huang² & Hui Xu^{1,2}

A series of phosphine oxide hosts, 4,6-bis(diphenylphosphoryl) dibenzothiophene (DBTDPO) and 4-diphenylphosphoryldibenzothiophene (DBTSPO), and electron transporting materials (ETM), 2-(diphenylphosphoryl)dibenzothiophene sulfone (2DBSOSPO), 3-(diphenylphosphoryl) dibenzothiophene sulfone (3DBSOSPO) and 4-(diphenylphosphoryl)dibenzothiophene sulfone (4DBSOSPO) were developed to support blue thermally activated delayed fluorescence (TADF) devices with high performance through optimizing intralayer and interlayer compatibility of emissive layers. On the basis of the triplet energy of ~3.0 eV for the hosts and ETMs, excitons can be effectively confined on DMAC-DPS. Compared to DBTSPO, DBTDPO can support the excellent distribution uniformity to blue TADF dye bis[4-(9,9-dimethyl-9,10-dihydroacridine) phenyl] sulfone (DMAC-DPS), owing to their configuration similarity; while 3DBSOSPO and 4DBSOSPO are superior in compatibility with the hosts due to the similar molecular polarity or configuration. Through adjusting the molecular configuration, the electrical performance of ETMs can be feasibly tuned, including the excellent electron mobility (μ_e) by the order of $10^{-3} \text{ cm}^2 \text{ V}^{-1} \text{ s}^{-1}$. As the result, DBTDPO and 4DBSOSPO endowed their four-layer blue TADF devices with the maximum current efficiency of 33.5 cd A^{-1} and the maximum external quantum efficiency more than 17%, which are impressive among the best blue TADF devices. It is showed that intralayer compatibility determines the maximum efficiencies, while interlayer compatibility influences efficiency stability.

Thermally activated delayed fluorescence (TADF) diodes have emerged in recent years as the third-generation organic light-emitting diodes, with the feature of harvesting triplet excitons through pure-organic TADF dyes with efficient reverse intersystem crossing (RISC)^{1–4}. Theoretically, TADF devices almost perfectly combine the respective advantages of fluorescence and phosphorescence organic light-emitting diodes (FLOLEDs and PHOLEDs) in economic and environmental protection and energy conservation, making this kind of light-emitting devices have a profound potential as high-efficiency artificial light sources^{5–10}.

Efficient RISC requires singlet-triplet splitting (ΔE_{ST}) between the first singlet (S_1) and triplet (T_1) energy levels as small as possible^{11–19}. In this case, the low-energy singlet charge transfer states (¹CT) are commonly utilized on the basis of strong electronic coupling in donor-acceptor (D-A) systems^{18–23}. However, the employment of D-A structures renders the high molecular polarity and strong intermolecular interactions for TADF dyes, remarkably worsening the quenching effects²⁴, e.g. triplet-triplet annihilation (TTA)^{25,26} and triplet-polaron quenching (TPQ)^{27,28}. Therefore, most of the efficient TADF devices adopt emitting layers (EML) with doping structures of TADF dyes dispersed in host matrixes^{29–33}. Similar to PHOLEDs, the utilization of triplet exciton not only endows the 100% theoretical internal quantum efficiency to TADF diodes, but also makes demands on excited-state characteristics of host materials, such as high T_1 energy for positive energy transfer to dopant and favourable charge injecting/transporting ability for effective charge carrier recombination³⁴. In consequence, many conventional phosphorescent host materials, such as N,N'-dicarbazolyl-4,4'-biphenyl (CBP)¹, 1,3-bis(carbazolyl)

¹Key Laboratory of Functional Inorganic Material Chemistry, Ministry of Education, Heilongjiang University, 74 Xuefu Road, Harbin 150080, P. R. China. ²Key Laboratory of Flexible Electronics (KLOFE) & Institute of Advanced Materials (IAM), Jiangsu National Synergetic Innovation Center for Advanced Materials (SICAM), Nanjing Tech University (NanjingTech), 30 South Puzhu Road, Nanjing 211816, P.R. China. Correspondence and requests for materials should be addressed to H.X. (email: hxu@hju.edu.cn)

benzene (*mCP*)³⁵ and bis[2-[di(phenyl)phosphino]-phenyl]ether oxide (*DPEPO*)³⁶, were adopted to realize the efficient red, green, blue and white TADF devices. Nevertheless, since T_1 value of blue TADF dyes is much higher than their phosphorescent counterparts, e.g. 2.9 eV of bis[4-(9,9-dimethyl-9,10-dihydroacridine)phenyl]sulfone (*DMAC-DPS*)³⁷ and 2.75 eV of bis(4,6-(difluorophenyl)pyridinato-*N,C*²)picolinate iridium(III) (*FIrpic*)³⁸, it is more challenging to develop high-energy-gap blue TADF host materials with favourable electroactivity. In addition, it is noteworthy that the high molecular polarity of TADF dyes also worsens the interactions with host materials, resulting in the serious host-dopant quenching^{39–41}. Ishimatsu and Adachi *et al.* demonstrated the reduction of photoluminescence quantum yield (PLQY) for TADF dyes in polar solvents, due to the increased nonradiative decay of S_1 state, which reflected the significant influence of the interactions between hosts and TADF dopants on luminescence performance of their solid solutions⁴². In this sense, a promising blue TADF host should possess the high T_1 energy, good electrical performance and host-dopant compatibility, viz. intralayer compatibility of EML.

On the other hand, the effective exciton confinement in EML for high electroluminescence (EL) efficiencies requires the T_1 energy of adjacent carrier transporting materials higher than that of dopants, among which the high-energy-gap electron transporting materials (ETM) are all along focused due to the contradiction between strong electron-withdrawing effect and high T_1 energy^{43–50}. To achieve the high electron affinity and mobility, ETMs should be established on polar groups, which either reduce excited energy or worsen interfacial interactions⁵¹. For TADF diodes, the sensitivity of TADF dyes to environmental polarity makes the interfacial interactions between host, dopant and ETM significant for device performance. On account of the charge carrier recombination zones close to EML/electron transporting layer (ETL) interfaces in the conventional hole-predominant devices, exciton can be quenched due to poor interlayer compatibility between EML and ETL, e.g. the formation of interfacial defects, dipole, charge/exciton traps and exciton-polaron interactions^{52–56}. In our recent work, it was showed that the interfacial interaction-induced quenching effect might be predominant to high efficiencies⁵⁷. Consequently, three prerequisites should be satisfied for high-performance blue TADF ETMs: (i) T_1 value approaching to 3.0 eV for exciton confinement; (ii) high electron affinity and mobility for charge flux balance and (iii) good compatibility with EML for suppressing interfacial quenching, viz. interlayer compatibility between EML and electron transporting layer (ETL). It is showed that the requirements on the properties of host and ETM are similar but rather difficult to be qualified simultaneously, especially for intralayer and interlayer compatibility of EML. In this case, it is imperative to figure out which one among these requirements is predominant and prioritized for molecular design.

In this contribution, two phosphine oxide hosts, 4,6-bis(diphenylphosphoryl)dibenzothiophene (*DBTDPO*) and 4-diphenylphosphoryldibenzothiophene (*DBTSPO*), collectively named *DBTxPO*, and three phosphine oxide ETMs, 2-(diphenylphosphoryl)dibenzothiophene sulfone (*2DBSOSPO*), 3-(diphenylphosphoryl)dibenzothiophene sulfone (*3DBSOSPO*) and 4-(diphenylphosphoryl)dibenzothiophene sulfone (*4DBSOSPO*), collectively named *mDBSOSPO*, were utilized to fabricate blue TADF devices with *DMAC-DPS* as dopant (Fig. 1). Exciton can be effectively confined on the emitter, in virtue of the high T_1 energy of *DBTxPO* and *mDBSOSPO* as ~3.0 eV. The frontier molecular orbital (FMO) levels of *mDBSOSPO* are accurately tuned by adjusting substitution position of their diphenylphosphine oxide (DPPO), accompanied with the excellent electron mobility (μ_e) by the order of 10^{-3} cm² V⁻¹ s⁻¹. Through optimizing the intralayer and interlayer compatibilities of EML, *DBTDPO* and *4DBSOSPO* endowed their four-layer blue TADF devices with the impressive performance of current efficiency (CE) up to 33.5 cd A⁻¹ and the maximum external quantum efficiency (EQE) beyond 17%. It is showed that the compatibility between host and dopant has predominant influence on the device efficiency, but the poor interlayer compatibility would worsen efficiency roll-offs due to the serious interfacial quenching effects. This work indicated the significance of intralayer and interlayer compatibility optimization and verified a feasible strategy of high-performance blue TADF diodes.

Results and Discussions

Design, Synthesis and Structures. The unique optoelectronic properties of *DBTxPO* make them superior as the hosts for blue TADF dyes. Their T_1 values are 2.98 and 2.90 eV to confine triplet excitons on *DMAC-DPS*. Their highest occupied molecular orbital (HOMO) and the lowest unoccupied molecular orbital (LUMO) levels are -6.0 and -2.5 eV. However, even through their dipole moments are also similar as ~4 Debye, symmetrically V-shaped *DBTDPO* is predominant to asymmetric *DBTSPO* in compatibility with *DMAC-DPS*, according to the “similarity-intermiscibility” theory. The surface morphology of the films of *DBTxPO* before and after *DMAC-DPS* doping can directly manifest host-dopant compatibility. The images of atom force microscopy (AFM) of the neat *vacuum*-evaporated films of *DBTxPO* (100 nm of thickness) showed the similar surface smoothness with almost equivalent root-mean-square roughness (R_s) of ~0.37 nm, while the film formability of *DMAC-DPS* was poor with R_s as large as 10 nm, which should be attributed to its strong intermolecular interaction induced aggregation (Fig. 2). After doping, the roughness of *DBTDPO:DMAC-DPS* film with concentration of 10%wt. was nearly unchanged, indicating the uniform dispersion of *DMAC-DPS* in *DBTDPO* matrix and their perfect compatibility. Contrarily, R_s of *DBTSPO:DMAC-DPS* film was about two folds of that of neat *DBTSPO* film. The aggregates of *DMAC-DPS* was formed in *DBTSPO* matrix, reflecting their different molecular symmetry induced poor compatibility.

The electron-donating dibenzothiophene (*DBT*) can be transformed to electron-withdrawing dibenzothiophene sulfone (*DBSO*) after oxidation of S atom. Therefore, the similar structures, different electrical characteristics and homology of *DBT* and *DBSO* can be utilized to construct hosts and ETMs with good compatibility. It is known that when bonding with strong electron-withdrawing groups, phosphine oxide (PO) groups can further polarize the molecules to enhance electrical performance and serve as bridge groups to assist charge transfer. Therefore, through varying DPPO substitution position, the intermolecular interactions between *DBSO* cores of adjacent *mDBSOSPO* molecules can be adjusted in virtue of steric effect of DPPO groups at different substitution positions, giving rise to their different electrical properties. Simultaneously, DPPO substitution positions

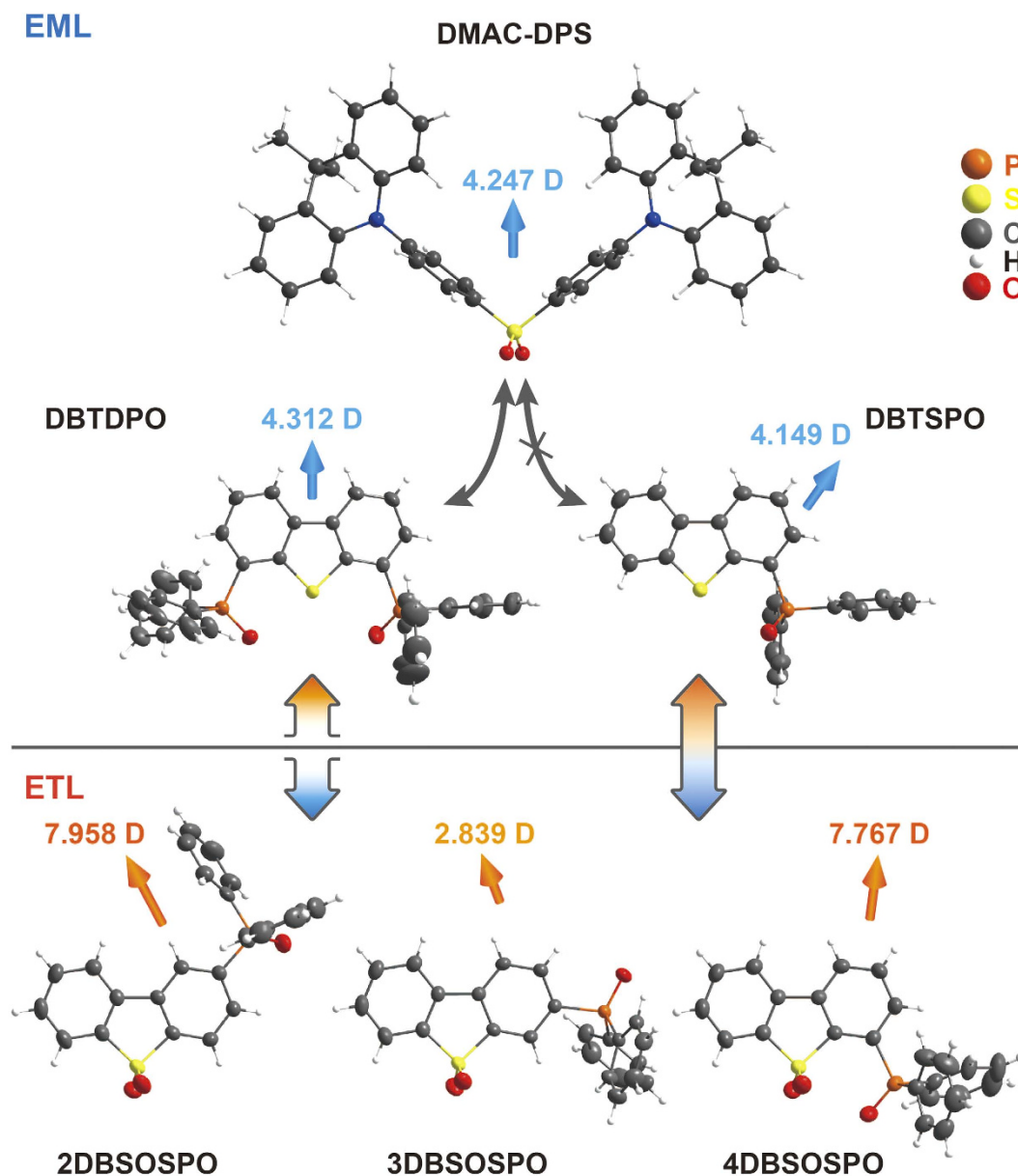


Figure 1. Chemical structures and dipole moments of single crystals of DBTxPO and *m*DBSOSPO, as well as those of DMAC-DPS.

determine the configurations of *m*DBSOSPO and thereby adjust interlayer compatibility with DBTxPO. According to molecular symmetry, *m*DBSOSPO should be more compatible with DBTSPO rather than DBTDPO, while DBTDPO is superior to DBTSPO in the compatibility with DMAC-DPS. This discrepancy between DBTxPO in intralayer and interlayer compatibility of EML can reflect which one is predominant to influence device performance.

*m*DBSOSPO can be conveniently synthesized from corresponding bromides of DBSO through Pd-catalyzed C-P coupling reaction with moderate total yields of 35–40%, respectively (Fig. 3). The structure characterization was established on the basis of mass spectrometry, NMR spectroscopy and elemental analysis. Their molecular structures are further confirmed by single crystal X-ray diffraction analysis (Fig. 1), in which only *m*DBSOSPO molecules are included. A close inspection reveals the π - π interactions between DBSO cores in adjacent 2DBSOSPO molecules with a short distance of 3.456 Å, which forms a direct and efficient channel for intermolecular electron hopping (Fig. 4a). The larger steric hindrance of DPPO groups at long axis of DBSO core in 3DBSOSPO enlarges the distance between adjacent DBSO cores to 6.659 Å. Nevertheless, two kinds of edge-to-face interactions between two adjacent DPPO groups and DBSO core are observed to establish electron transfer channels with the assistance of DPPO as bridge groups (Fig. 4b). Different to 2DBSOSPO and 3DBSOSPO with single molecular orientation, two kinds of 4DBSOSPO molecules exist in its packing diagram (Fig. 4c), in which two parallel 4DBSOSPO molecules are partitioned by one vertical 4DBSODPO molecule.

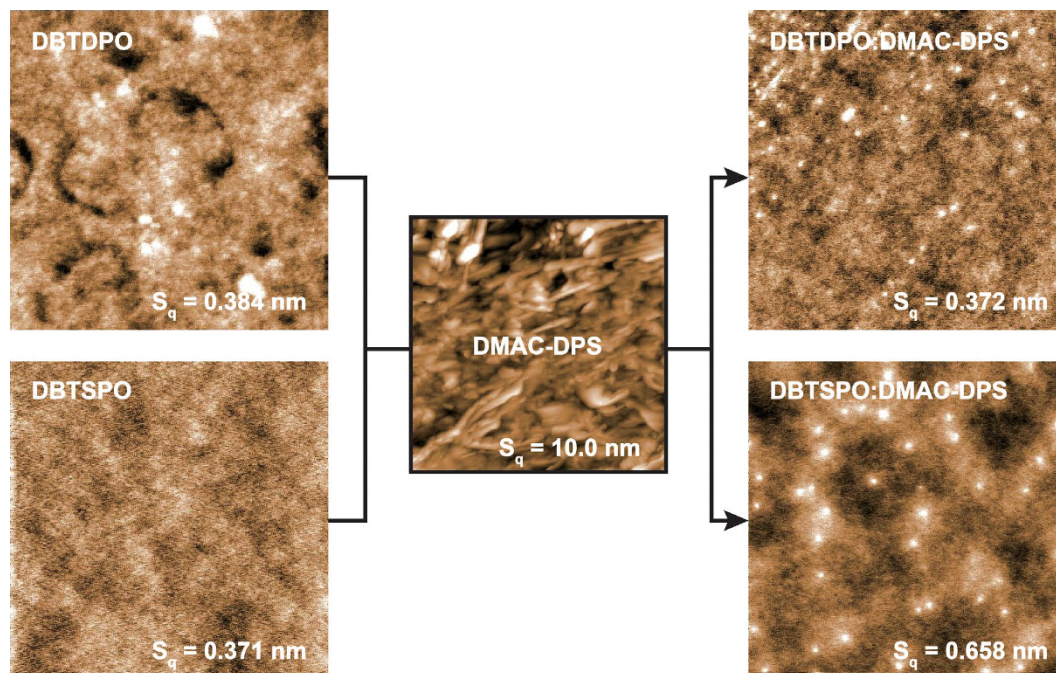


Figure 2. AFM images of vacuum-evaporated thin films of *m*DBSOSPO with thickness of 100 nm before (left) and after (right) DMAC-DPS doping.

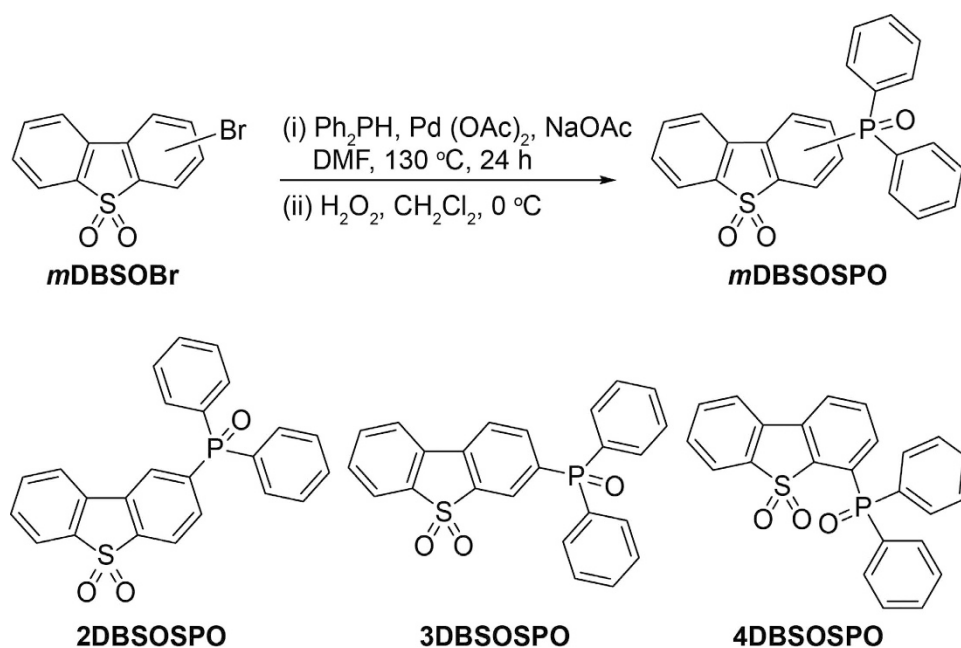


Figure 3. Synthetic procedure of *m*DBSOSPO ($m = 2, 3$ and 4).

There are a series of $S=O \dots H$ and edge-to-face interactions formed between vertical and parallel **4DBSODPO** molecules, making the former serve as interchange of intermolecular electron hopping. As expected, the different substitution position of DPPO results in the different intermolecular interaction in *m*DBSOSPO, thereby rendering their different electron hopping processes. The **DBSO**-centered channel in **2DBSOSPO** facilitates the direct, consistent and rapid electron transfer. **3DBSOSPO** showed two kinds of electron hopping paths as **DBSO** \rightarrow **DPPO** \rightarrow **DBSO** and **DBSO** \rightarrow **DPPO** \rightarrow **DPPO** \rightarrow **DBSO** with one or two DPPOs as bridge groups. The electron migration in **4DBSOSPO** is the most complicated with multiple mutual **DBSO** \rightarrow **DPPO** electron hopping. It is rational that the effective electron transportation is in direct proportion to continuity and coherence of intermolecular electron hopping. In this sense, just according to intermolecular interactions, **2DBSOSPO** should be superior in electron transportation among *m*DBSOSPO.

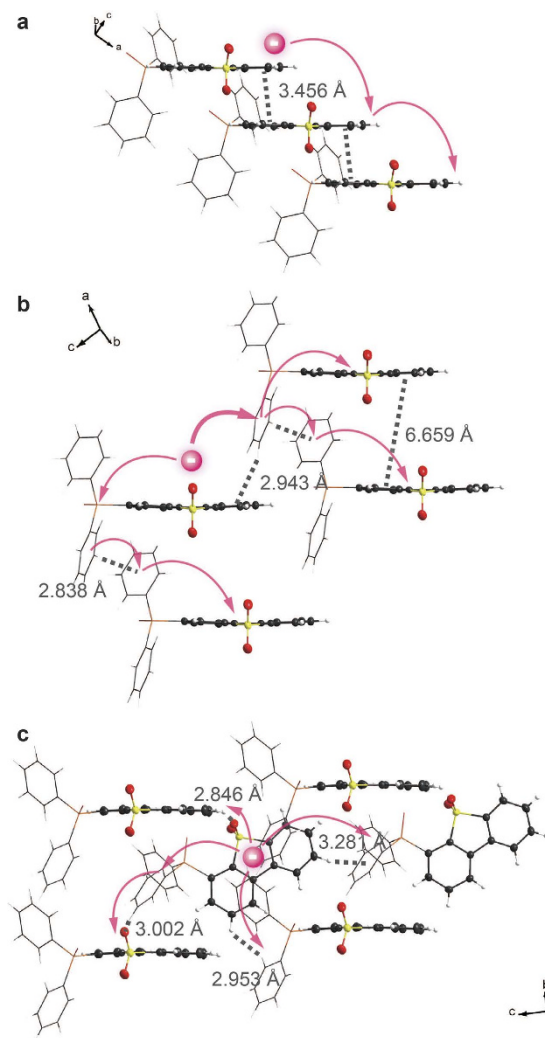


Figure 4. Packing diagrams of 2DBSOSPO (a) 3DBSOSPO (b) and 4DBSOSPO (c) in which DPPOs were drawn in tube mode for clarity, and their presumed intermolecular electron migration processes according to the intermolecular interactions.

Differential scanning calorimetry (DSC) and thermogravimetric analysis (TGA) of *m*DBSOSPO were performed to investigate their thermal properties (Figure S1 and Table 1). Both the temperature of glass transition (T_g) and melting point (T_m) of 2DBSOSPO were observed at 151 and 221 °C, indicating its improved morphological stability. T_m of 3DBSOSPO decreases to 211 °C, in accord with its weaker intermolecular interactions. However, 4DBSOSPO revealed the highest T_m of 264 °C, which should be ascribed to the strong S = O...H interactions. In addition, the decomposition temperatures (T_d) at weight loss of 5% for *m*DBSOSPO were similar as 370 °C, high enough to make device fabrication through *vacuum* evaporation feasible. Different to 2DBSOSPO and 3DBSOSPO with single decomposition process, two weight-loss steps were observed for 4DBSOSPO, indicating its stronger rigidity and intramolecular interactions between DBSO and DPPO.

Optical Properties. The optical properties of DBT*x*PO are identical with the same fluorescence and phosphorescence spectra. The large-range spectroscopic overlaps between their PL spectra and the absorption spectrum of DMAC-DPS from 320 to 400 nm support the efficient energy transfer (Fig. 5a), which is further verified by the identical DMAC-DPS-attributed emissions with peaks at 482 nm from *vacuum*-evaporated DBT*x*PO:DMAC-DPS films. However, PLQY of DBTDPO:DMAC-DPS film reaches to 87%, which is remarkably higher than 75% of DBTSPO:DMAC-DPS film. The transient PL spectra of these films shows the major contribution of delayed fluorescence component to the sky-blue emissions (inset in Fig. 5a). However, the lifetime of delayed fluorescence (τ_{DF}) for DBTSPO:DMAC-DPS is 22.9 μ s, about 2 folds of that of DBTDPO:DMAC-DPS (11.5 μ s). Both smaller PLQY and longer τ_{DF} of DBTSPO:DMAC-DPS film should be attributed to the remarkable aggregation of DMAC-DPS, as indicated by its AFM image (Fig. 2). The too long emission lifetime would worsen the quenching effect in DBTSPO:DMAC-DPS, let alone its inferiority in PLQY.

Electronic absorption spectra of *m*DBSOSPO in dilute solutions (10^{-6} mol L⁻¹ in CH₂Cl₂) are almost identical to that of DBSO, except for the peaks at 230 nm attributed to $\pi \rightarrow \pi^*$ transition of DPPO (Fig. 5b and Table 1). 4DBSODPO showed the least absorption peaks, in accord with its most rigid structure. The S₁ energy

Compound	Absorption (nm)	Emission (nm)	S ₁ (eV)	T ₁ (eV)	T _g /T _m /T _d (°C)	HOMO (eV)	LUMO (eV)	RE ^g (eV)	μ _e ^h (cm ² /V/s)
DBSO	324, 291, 278, 269, 242, 234, 228 ^a , 337, 283, 205 ^b	358 ^a 402 ^b	3.60 ^c 4.85 ^d	3.00 ^c 2.86 ^d	—/—/207	−6.56 ^f −6.67 ^d	−3.08 ^f −1.82 ^d	0.4261	—
2DBSODPO	330, 282, 249, 240, 227 ^a , 335, 294, 285, 275, 254 ^b	371 ^a 381 ^b	3.51 ^c 4.77 ^d	2.98 ^c 2.82 ^d	151/221/367	−7.10 ^f −6.76 ^d	−3.29 ^f −1.99 ^d	0.5505	3.96 × 10 ^{−3}
3DBSODPO	325, 298, 285, 249, 241, 228 ^a , 334, 303, 290, 277, 255, 246 ^b	365 ^a 378 ^b	3.53 ^c 4.71 ^d	2.99 ^c 2.80 ^d	—/—211/373	−7.05 ^f −6.74 ^d	−3.31 ^f −2.03 ^d	0.5075	3.69 × 10 ^{−3}
4DBSODPO	332, 282, 228 ^a 335, 296, 282, 253 ^b	371 ^a 375 ^b	3.51 ^c 4.85 ^d	2.97 ^c 2.87 ^d	—/—262/375	−7.09 ^f −6.63 ^d	−3.14 ^f −1.78 ^d	0.5291	1.45 × 10 ^{−3}

Table 1. Physical properties of DBSO derivatives. ^aIn CH₂Cl₂ (10^{−6} mol L^{−1}); ^bin film; ^cestimated according to the absorption edges; ^dDFT calculated results; ^ecalculated according to the 0–0 transitions of the phosphorescence spectra; ^fcalculated according to the equation HOMO/LUMO = 4.78 + onset voltage⁶⁰; ^greorganization energy of electron; ^helectron mobility estimated by *I*-*V* characteristics of electrononly devices according filed-dependent SCLC model⁶¹.

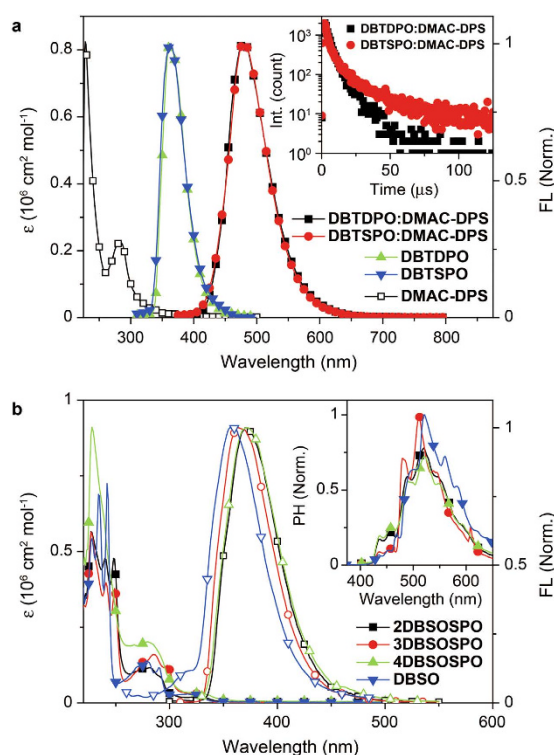


Figure 5. (a) UV absorption spectrum of DMAC-DPS, PL spectrum of DBTxPO and steady-state emission spectra and time-decay curves (inset) of DMAC-DPS in DBTxPO:DMAC-DPS (10%wt.) thin films; (b) Electronic absorption and fluorescence (FL) spectra of *m*DBSOSPO and DBSO in CH₂Cl₂ (10^{−6} mol L^{−1}) and low-temperature phosphorescence (PH) spectra (inset) by time-resolved technology after a delay of 300 μs.

of *m*DBSOSPO is estimated as ~3.5 eV, only 0.1 eV less than that of DBSO. The situation of fluorescence spectra for *m*DBSOSPO is similar that the emission profiles are identical with bathochromic shifts of about 7–13 nm compared to that of DBSO, which should be attributed to the electron-withdrawing effect of DPPO. However, the DPPO substitution hardly influences the characteristics of triplet excited state that all of the compounds exhibit the almost overlapped phosphorescence spectra, indicating their same T₁ locations on DBSO cores. According to 0–0 transitions at ~415 nm, the T₁ energy of *m*DBSOSPO is estimated as ~3.0 eV, which is high enough to

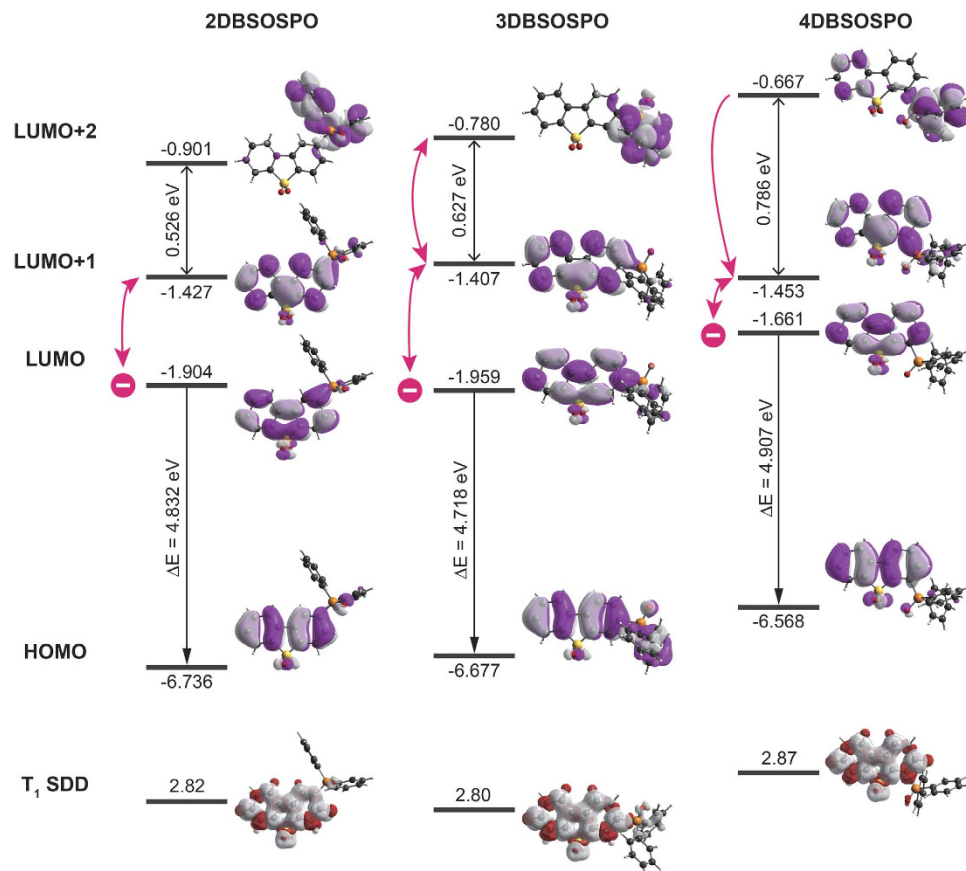


Figure 6. Contours and energy levels of frontier molecular orbitals and spin density distributions of triplet states for *m*DBSOSPO.

effectively confine excitons in EML. The identical optical properties of *DBT**x**PO* and *m*DBSOSPO exclude the interference from the different energy transfer and exciton diffusion suppression efficacies on their device performance.

DFT Simulation. To figure out the nature of electronic characteristics of *m*DBSOSPO, their ground states and T₁ states were optimized at the level of B3LYP/6-31g* with density function theory (DFT) simulation (Fig. 6 and Table 1). It is known that the frontier molecular orbitals (FMO) make the major contributions to charge gain or loss, which reflect the charge affinity and migration possibility.

The HOMO and LUMO of *m*DBSOSPO are mainly localized on their DBSO cores, in accord with their similar optical properties, which further verify their unipolar characteristics. It is noteworthy that 3DBSOSPO shows the deepest LUMO at -1.959 eV, slightly lower than -1.904 eV of 2DBSOSPO, while the tendency of their HOMO is opposite. The HOMO and LUMO of 4DBSOSPO are the shallowest among *m*DBSOSPO. This should be attributed to the minimal involvement of 4-C in these orbitals, rendering the smallest influence of 4-substituted DPPO on FMO energy levels. As the result, the HOMO-LUMO energy gap of 4DBSOSPO is the biggest, while that of 3DBSOSPO is the smallest, which is owing to the slight conjugation extension by P=O substituted at long axis of DBSO core. Therefore, 2DBSOSPO and 3DBSOSPO have the excellent electron injecting ability, much stronger than that of 4DBSOSPO.

The electron cloud distributions of the LUMO and LUMO + 1 orbitals for *m*DBSOSPO are thoroughly localized on DBSO core, except for 3DBSOSPO, whose LUMO partially extends to its DPPO; while their DPPO groups make the major contributions to their LUMO + 2 orbitals. Therefore, the predominant electron capture sites for *m*DBSOSPO are DBSO cores, accompanied with DPPOs as transitional peripheral groups. In this sense, according to the single-crystal packing diagram of 2DBSODPO (Fig. 4), with the effective intermolecular DBSO-DBSO interaction formed continuous electron hopping channel, its electron transporting ability should be the strongest among *m*DBSOSPO. Contrarily, intermolecular electron hopping in 3DBSOSPO and 4DBSOSPO depends on their DPPOs as bridge groups. Owing to the involvement of DPPO in the LUMO (Fig. 4), the bidirectional electron migration between DPPO and DBSO in 3DBSOSPO should be facile, also supporting a continuous energy hopping channel. However, for 4DBSOSPO, the huge energy gap of 0.786 eV between LUMO + 1 and LUMO + 2 and the exclusion of DPPO in its LUMO render the unidirectional electron migration from DPPO to DBSO. It is rational that with the continuous electron hopping processes, 2DBSOSPO and 3DBSOSPO should be superior to 4DBSOSPO in electron transportation.

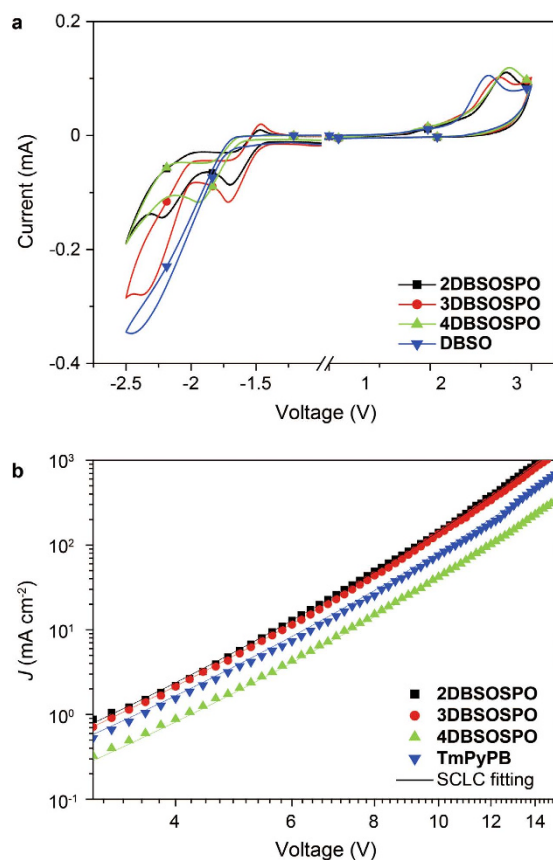


Figure 7. (a) Cyclic voltammograms of *m*DBSOSPO and DBSO measured in CH_2Cl_2 at room temperature with tetrabutylammonium hexafluorophosphate (0.1 M) as electrolyte under the scanning rate of 100 mV s^{-1} ; (b) volt-ampere characteristics of *m*DBSOSPO and TmPyPB based electron-only devices.

Spin density distribution (SDD) of T_1 states of *m*DBSOSPO shows their identical T_1 locations on DBSO cores, which afford their similar T_1 value of $\sim 2.8 \text{ eV}$, in accord with optical analysis data (Table 1). The similar optical properties, e.g. the HOMO-LUMO energy gaps and T_1 energy, of *m*DBSOSPO should be ascribed to the same DBSO-localized FMO and T_1 states. Simultaneously, substitution position of DPPO remarkably influences the FMO energy levels and extension, which render the different electrical properties of *m*DBSOSPO.

Electrical Performance. The electron affinity and hole blocking ability of *m*DBSOSPO were evaluated by their electrochemical redox behaviors, according to the cyclic voltammogram (Fig. 7a). Compared to DBSO, the irreversible DBSO-originated anodic peaks of *m*DBSOSPO shift to higher potentials with the onset voltages as high as $\sim 2.3 \text{ V}$, corresponding to the extremely deep LUMO at -7.0 eV , which were even 0.3 eV lower than that of conventional hole-blocking material 2,9-Dimethyl-4,7-diphenyl-1,10-phenanthroline (BCP) (Table 1). In contrast to DBSO with single irreversible reduction peak, *m*DBSOSPO showed two cathodic peaks, corresponding to the reduction of DBSO core and DPPO, respectively. Estimated with the onset voltages, the LUMO level of 4DBSOSPO is -3.14 eV , only 0.06 eV lower than that of DBSO; while, the LUMO levels of 2DBSOSPO and 3DBSOSPO are dramatically reduced to about -3.3 eV , revealing their excellent electron injecting ability. It is noteworthy that contrary to the irreversible peaks of 4DBSOSPO, owing to the electron-withdrawing inductive effect of DPPO at 2 and 3 positions, the DBSO-attributed peaks of 2DBSOSPO and 3DBSOSPO become reversible, indicating their stable and cyclical electron capture ability.

As ETMs, the electron mobility of *m*DBSOSPO is one of the most important indicators. The single-layer nominal electron-only devices of *m*DBSOSPO were fabricated with configuration of ITO|LiF (1 nm)|*m*DBSOSPO (100 nm)|LiF (1 nm)|Al to estimate their intrinsic electron transporting ability, where LiF served as electron-injecting layers. Volt-ampere characteristics of these electron-only devices are shown in Fig. 7b. The current density (J) of 4DBSOSPO-based devices was the lowest at the same voltages among these devices; while, 2DBSOSPO and 3DBSOSPO endowed their devices with the similar I - V curves. The stronger electron transporting ability of 2DBSOSPO and 3DBSOSPO can be owing to their higher electron affinity and the continuous intermolecular electron hopping channels, as demonstrated by DFT simulation and single-crystal results. Significantly, according to the model of field-dependent space charge limited current (FD-SCLC), electron mobility (μ_e) of *m*DBSOSPO were estimated as high as 3.96×10^{-3} , 3.69×10^{-3} and $1.45 \times 10^{-3} \text{ cm}^2 \text{ V}^{-1} \text{ s}^{-1}$, respectively (Table 1). The mobility of 2DBSOSPO and 3DBSOSPO was even higher than that of the most popular

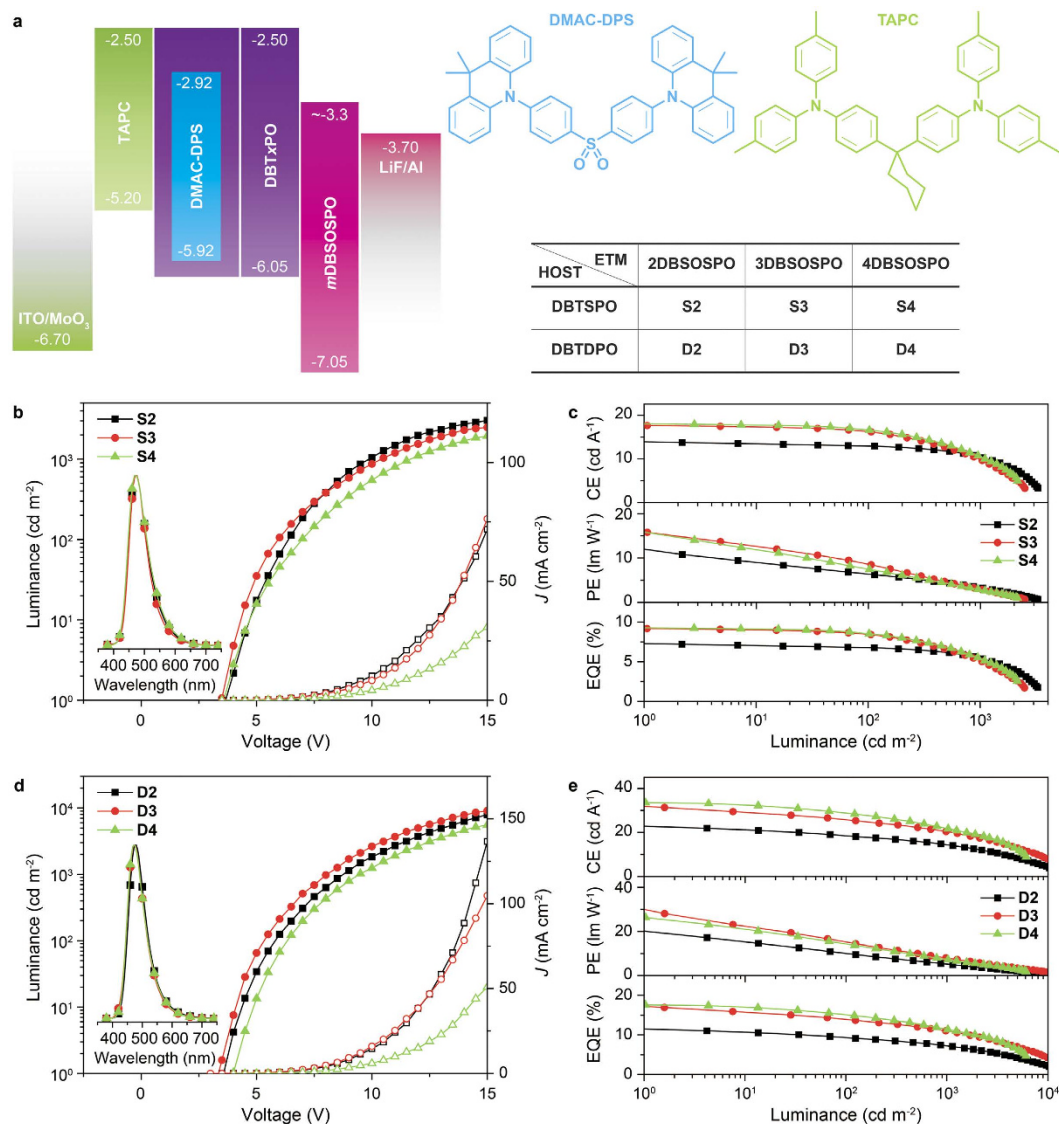


Figure 8. (a) Device structure and energy level diagram of DMAC-DPS based blue TADF OLEDs; (b,d) Luminance-current density (J)-voltage characteristics and (c and e) efficiencies-luminance curves of *m*DBSOSPO-based blue TADF devices (b,c) for DBTSPO-based devices S2–S4; while (d,e) for DBTDPO-based devices D2–D4).

ETM 1,3,5-tri[(3-pyridyl)-phen-3-yl]benzene (**TmPyPB**) with high triplet energy, making them outstanding among high-energy-gap ETMs reported so far.

Therefore, in accord with DFT simulation results and intermolecular interactions, **2DBSOSPO** and **3DBSOSPO** show their superiority in electron injection and transportation. The correlation of the substitution position of DPPO and its inductive effect and intermolecular interactions can be utilized to feasibly modulate electrical properties at the same time of configuration adjustment. With the LUMO lower than -3.0 eV and the electron mobility by the level of 10^{-3} $\text{cm}^2 \text{V}^{-1} \text{s}^{-1}$, the charge flux balance in EML of *m*DBSOSPO-based device can be expected.

EL performance of blue TADF devices. To figure out the influence of intralayer and interlayer compatibility on EL performance of blue TADF diodes, two series of devices were fabricated with a four-layer configuration of ITO|MoO₃ (8 nm)|TAPC (70 nm)|DBTxPO:DMAC-DPS (10%, 20 nm)|DBTxPO (5 nm)|*m*DBSOSPO (35 nm)|LiF (1 nm)|Al, in which TAPC was di-[4-(N,N-ditolyl-amino)-phenyl]cyclohexane as hole transporting layer. A neat DBTxPO layer was inserted between EML and ETL to alleviate interfacial effects, whose thickness was optimized as 5 nm in order to confine exciton in EML. Therefore, when DBTSPO served as host, the devices S2, S3 and S4, collectively named S_n, used 2DBSOSPO, 3DBSOSPO and 4DBSOSPO as electron transporting layer, respectively; while, devices D2, D3 and D4, collectively named D_n, employed DBTDPO as the host (Fig. 8a). The vertical comparison between two series of devices with different hosts reflected the influence of intralayer compatibility of EML on EL performance. Meanwhile, on account of the identical optical properties of

mDBSOPO, horizontal comparative research on the differences in EL performance of each device series should be attributed to the discrepancy of **mDBSOPO** in electrical characteristics and compatibility with host. All of the devices showed the pure emissions from **DMAC-DPS** with peaks at 472 nm, revealing the effective exciton confinement on the dopant by the high T_1 energy of **DBTxPO** and **mDBSOPO** (insets in Figs 7d and 8b).

The driving voltages of **S3** was the lowest among **Sn** as 3.5 V for onset and 6.0 V at 100 cd m^{-2} (Fig. 8b and Table S1), which were 0.5 V lower than those of **S2**. However, when driving voltage exceeded 8 V, the luminance of **S2** was larger than that of **S3**. **S4** revealed the highest driving voltages, which were 0.5–1.5 V higher than those of **S3**. The tendency of driving voltages for **Dn** was similar that **D3** showed the lowest driving voltages of 3.5 V for onset, 5.5 and 8.5 V at 100 and 1000 cd m^{-2} , which were 0.5 V lower than those of **D2** and 1 V lower than those of **D4** (Fig. 8d and Table S1). Simultaneously, J of **Sn** was in the order of **S2** \approx **S3** $>$ **S4**, which was similar to the situation of **Dn**. Therefore, the driving voltage and charge flux in the devices were coincident with the electron affinity and μ_e of the corresponding ETM **mDBSOPO**, which implies the majority carrier of hole in these devices and recombination zone adjacent the interface between EML and ETL. In this case, the suppression of interfacial quenching would be crucial to high efficiencies. In this case, it is noticeable that when J more than 8.5 mA cm^{-2} , the luminance of **S3** turned to less than that of **S2**, indicating the more serious quenching for the combination of **DBTSPO** and **3DBSOPO**.

The efficiencies directly showed the effect of interlayer and intralayer compatibility on the device performance (Figs. 7d and 8c and Table S1). The maximum efficiencies of **S3** and **S4** were comparable as 17.6 and 17.9 cd A^{-1} for CE, 15.8 and 14.1 lm W^{-1} for power efficiency (PE) and 9.2% for EQE, which were much higher than those of **S2** as 13.7 cd A^{-1} , 10.8 lm W^{-1} and 7.2%. The lowest efficiencies of **S2** should be attributed to the worst compatibility between **2DBSOPO** and **DBTSPO** regarding to their opposite configurations and much different polarity. It is also noteworthy that in spite of its worst electrical performance, **4DBSOPO** still endowed its devices with the high efficiencies, in virtue of its strongest compatibility with *ortho*-linked **DBTxPO**. Nevertheless, the efficiency roll-offs of **S2** were the lowest as 6 and 25% for CE, 43 and 70% for PE and 6 and 25% for EQE at 100 and 1000 cd m^{-2} , respectively, which should be owing to its most balanced charge flux supported by **2DBSOPO**. The situation for **Dn** was similar that **D3** and **D4** revealed the similar maximum efficiencies of 31.3 and 33.5 cd A^{-1} , 28.1 and 26.3 lm W^{-1} and 16.9 and 17.4%, respectively, which were about 1.5 folds of those of **D2**. Differently, the efficiency roll-offs of **Dn** were almost the same as 15 and 35% for CE, 45 and 70% for PE and 15 and 35% for EQE at 100 and 1000 cd m^{-2} , respectively, which was originated from their similar interfacial quenching effects due to the incompatibility between **DBTDPO** and **mDBSOPO**. Simultaneously, at 100 cd m^{-2} , **DBTSPO** supported its devices **Sn** with the efficiency roll-offs only a half of those of **Dn**, which was obviously owing to the suppressed interfacial quenching by favorable compatibility between **DBTSPO** and **mDBSOPO**. Nevertheless, compared with **Sn**, **DBTDPO** endowed **Dn** with the maximum efficiencies dramatically improved for 50%, correspondingly, which should be ascribed to the stronger compatibility between **DBTDPO** and **DMAC-DPS**. Then, due to their limited luminance at high J , the efficiency roll-offs of **S3** and **S4** at 1000 cd m^{-2} became higher than those of **Dn**. The combined utilization of **DBTDPO** as host and **3DBSOPO** or **4DBSOPO** as ETM endowed their devices with the impressive EL performance, e.g. the maximum EQE beyond 15%, among the best blue TADF devices reported so far.

In general, the higher efficiencies of **Dn** than those of **Sn** manifested that the intralayer compatibility between host and dopant is the primary issue should be considered. Meanwhile, the interlayer compatibility between EML and ETL would have remarkable influence on the efficiency stability, as indicated by the lower efficiency roll-offs at 100 cd m^{-2} of **Sn** than those of **Dn**.

Conclusions

A series of dibenzothiophene-based hosts and ETMs **DBTxPO** and **mDBSOPO** were utilized to realize high-performance blue TADF devices with optimized intralayer and interlayer compatibility. AFM images showed the more uniform dispersion of **DMAC-DPS** in **DBTDPO**, revealing their stronger compatibility, which further endows **DBTDPO:DMAC-DPS** films with the higher PLQY and reduced emission lifetime. The optical properties of **mDBSOPO** are well-controlled with similar S_1 and T_1 for effective exciton confinement in EML, while, their electrical properties are enhanced by DPPO substitution position, rendering the LUMO levels lower than -3.0 eV for effective electron injection and high μ_e by the order of 10^{-3} $\text{cm}^2 \text{V}^{-1} \text{s}^{-1}$. Through employing **DBTDPO** as host and **3DBSOPO** or **4DBSOPO** as ETM, the impressive EL performance, e.g. the maximum EQE beyond 17%, were realized, which was among the best results for blue TADF devices. On the basis of comprehensive comparison on the influence of host and ETM variation on the EL performances, it is showed that intralayer compatibility between host and dopant is the primary determinant of device efficiencies due to its correlation with EML-inside quenching. Simultaneously, the interlayer compatibility between EML and ETL would influence the interfacial quenching effects, thereby having remarkable effects on efficiency roll-off reduction. This work verified the significance of host-dopant compatibility and interfacial optimization on developing high-performance blue TADF diodes.

Methods

Materials and Instruments. All the reagents and solvents used for the synthesis of the compounds were purchased from Aldrich and Acros companies and used without further purification.

^1H NMR spectra were recorded using a Varian Mercury plus 400 NB spectrometer relative to tetramethylsilane (TMS) as internal standard. Molecular masses were determined by a FINNIGAN LCQ Electro-Spraying Ionization-Mass Spectrometry (ESI-MS), or a MALDI-TOF-MS. Elemental analyses were performed on a Vario EL III elemental analyzer. The crystal suitable for single-crystal XRD analysis was obtained through slowly diffusing hexane into dichloromethane solution of **mDBSOPO** at room temperature. All diffraction data were collected at 295 K on a Rigaku Xcalibur E diffractometer with graphite monochromatized Mo $K\alpha$ ($\lambda = 0.71073$ Å)

radiation in ω scan mode. All structures were solved by direct method and difference Fourier syntheses. Non-hydrogen atoms were refined by full-matrix least-squares techniques on F2 with anisotropic thermal parameters. The hydrogen atoms attached to carbons were placed in calculated positions with C–H = 0.93 Å and U(H) = 1.2 Ueq(C) in the riding model approximation. All calculations were carried out with the SHELXL97 program. Absorption and photoluminescence (PL) emission spectra of the target compound were measured using a SHIMADZU UV-3150 spectrophotometer and a SHIMADZU RF-5301PC spectrophotometer, respectively. Thermogravimetric analysis (TGA) and differential scanning calorimetry (DSC) were performed on Shimadzu DSC-60A and DTG-60A thermal analyzers under nitrogen atmosphere at a heating rate of 10 °C min⁻¹. Cyclic voltammetric (CV) studies were conducted using an Eco Chemie B. V. AUTOLAB potentiostat in a typical three-electrode cell with a platinum sheet working electrode, a platinum wire counter electrode and a silver/silver chloride (Ag/AgCl) reference electrode. Tetrabutylammonium hexafluorophosphate was used as electrolyte with a concentration of 0.1 mol L⁻¹. All electrochemical experiments were carried out under a nitrogen atmosphere at room temperature in dichloromethane. Phosphorescence spectra were measured in dichloromethane using an Edinburgh FPLS 920 fluorescence spectrophotometer at 77 K cooling by liquid nitrogen with a delay of 300 μ s using Time-Correlated Single Photon Counting (TCSPC) method with a microsecond pulsed Xenon light source for 10 μ s–10 s lifetime measurement involving scatterer for correction, the synchronization photomultiplier for signal collection and the Multi-Channel Scaling Mode of the PCS900 fast counter PC plug-in card for data processing.

General procedure of Pd-catalyzed P-C coupling. In Ar₂, 2.95 g (10 mmol) of *m*DBSOBr, 1.23 g of NaOAc (15 mmol), 0.0112 g of Pd(OAc)₂ (0.05 mmol) and 2.63 mL of Ph₂PH (15 mmol) were dissolved in 25 mL of DMF. The mixture was stirred for 24 h at 130 °C. The reaction was then quenched by adding 25 mL of water, and extracted with 3 × 25 mL of CH₂Cl₂. The organic layer was combined, concentrated to 10 mL and cooled to 0 °C. Then, 4 mL of 30% H₂O₂ was added to the mixture and stirred for 8 h. The system was extracted with 3 × 10 mL of CH₂Cl₂. The organic layer was dried with anhydrous sodium sulfate. The solvent was removed in *vacuo*. The residue was purified by flash column chromatography to the title compounds.

2-(diphenylphosphoryl)dibenzothiophene sulfone (2DBSOSPO): white powder with a yield of 40%. ¹H NMR (TMS, CDCl₃, 400 M Hz): δ = 8.392 (d, *J* = 11.6 Hz, 1H), 7.854 (q, *J*₁ = 9.0, *J*₂ = 17.0 Hz, 3H), 7.683 (q, *J*₁ = 7.8, *J*₂ = 13.0 Hz, 5H), 7.602 (m, 4H), 7.544 ppm (t, *J* = 7.4 Hz, 4H); LDI-TOF: *m/z* (%): 416 (100) [M⁺]; elemental analysis (%) for C₂₄H₁₇O₃PS: C 69.22, H 4.11, O 11.53, S 7.70; found: C 69.25, H 4.09, O 11.65, S 7.77.

3-(diphenylphosphoryl)dibenzothiophene sulfone (3DBSOSPO): white powder with a yield of 35%. ¹H NMR (TMS, CDCl₃, 400 M Hz): δ = 8.148 (t, *J* = 9.6 Hz, 1H), 7.941 (t, *J* = 5.6 Hz, 2H), 7.844 (t, *J* = 8.4 Hz, 2H), 7.680 (q, *J*₁ = 7.0, *J*₂ = 12.2 Hz, 5H), 7.600 (m, 3H), 7.513 (t, *J* = 7.4 Hz, 4H); LDI-TOF: *m/z* (%): 416 (100) [M⁺]; elemental analysis (%) for C₂₄H₁₇O₃PS: C 69.22, H 4.11, O 11.53, S 7.70; found: C 69.23, H 4.11, O 11.70, S 7.81.

4-(diphenylphosphoryl)dibenzothiophene sulfone (4DBSOSPO): white powder with a yield of 35%. ¹H NMR (TMS, CDCl₃, 400 M Hz): δ = 7.997 (d, *J* = 2.8 Hz, 1H), 7.795 (q, *J*₁ = 7.6, *J*₂ = 12.0 Hz, 5H), 7.693 (q, *J*₁ = 8.4, *J*₂ = 18.0 Hz, 3H), 7.587 (t, *J* = 6.8 Hz, 3H), 7.493 (t, *J* = 7.4 Hz, 5H); LDI-TOF: *m/z* (%): 416 (100) [M⁺]; elemental analysis (%) for C₂₄H₁₇O₃PS: C 69.22, H 4.11, O 11.53, S 7.70; found: C 69.25, H 4.13, O 11.68, S 7.76.

DFT Calculations. DFT computations were carried out with different parameters for structure optimizations and vibration analyses. The ground states and triplet states of molecules in vacuum were optimized with assistance of single crystal structures by the restricted and unrestricted formalism of Beck's three-parameter hybrid exchange functional⁵⁸ and Lee, and Yang and Parr correlation functional⁵⁹ (B3LYP)/6–31G(d) respectively. The fully optimized stationary points were further characterized by harmonic vibrational frequency analysis to ensure that real local minima had been found without imaginary vibrational frequency. The total energies were also corrected by zero-point energy both for the ground state and triplet state. The Spin Density Distributions were visualized with Gaussview 3.0. All computations were performed using the Gaussian 03 package.

Device Fabrication and Testing. Before loading into a deposition chamber, the ITO substrate was cleaned with detergents and deionized water, dried in an oven at 120 °C for 4 h, and treated with oxygen plasma for 3 min. Devices were fabricated by evaporating organic layers at a rate of 0.1–0.2 nm s⁻¹ onto the ITO substrate sequentially at a pressure below 4 × 10⁻⁴ Pa. Onto the electron-transporting layer, a layer of LiF with 1 nm thickness was deposited at a rate of 0.1 nm s⁻¹ to improve electron injection. Finally, a 100-nm-thick layer of Al was deposited at a rate of 0.6 nm s⁻¹ as the cathode. The emission area of the devices was 0.09 cm² as determined by the overlap area of the anode and the cathode. After fabrication, the devices were immediately transferred to a glove box for encapsulation with glass cover slips using epoxy glue. The EL spectra and CIE coordinates were measured using a PR655 spectra colorimeter. The current-density-voltage and brightness-voltage curves of the devices were measured using a Keithley 4200 source meter and a calibrated silicon photodiode. All the measurements were carried out at room temperature under ambient conditions. For each structure, five devices were fabricated to confirm the performance repeatability. To make conclusions reliable, the data reported herein were most close to the average results.

References

- Uoyama, H. *et al.* Highly efficient organic light-emitting diodes from delayed fluorescence. *Nature* **492**, 234–238 (2012).
- Tao, Y. *et al.* Thermally Activated Delayed Fluorescence Materials Towards the Breakthrough of Organoelectronics. *Adv Mater* **26**, 7931–7958 (2014).
- Endo, A. *et al.* Thermally Activated Delayed Fluorescence from Sn4+ -Porphyrin Complexes and Their Application to Organic Light-Emitting Diodes - A Novel Mechanism for Electroluminescence. *Adv Mater* **21**, 4802–4806 (2009).
- Graves, D., Jankus, V., Dias, F. B. & Monkman, A. Photophysical Investigation of the Thermally Activated Delayed Emission from Films of m-MTDATA:PBD Exciplex. *Adv Funct Mater* **24**, 2343–2351 (2014).
- Xu, H. *et al.* Recent progress in metal-organic complexes for optoelectronic applications. *Chem Soc Rev* **43**, 3259–3302 (2014).

6. Adachi, C. Third-generation organic electroluminescence materials[†]. *Jap J Appl Phys* **53**, 060101 (2014).
7. Higuchi, T., Nakanotani, H. & Adachi, C. High-Efficiency White Organic Light-Emitting Diodes Based on a Blue Thermally Activated Delayed Fluorescent Emitter Combined with Green and Red Fluorescent Emitters. *Adv Mater* **27**, 2019–2023 (2015).
8. Zhang, D. *et al.* Highly efficient and color-stable hybrid warm white organic light-emitting diodes using a blue material with thermally activated delayed fluorescence. *J Mater Chem C* **2**, 8191–8197 (2014).
9. Cho, Y. J., Yook, K. S. & Lee, J. Y. Cool and warm hybrid white organic light-emitting diode with blue delayed fluorescent emitter both as blue emitter and triplet host. *Sci Rep* **5**, 7859 (2015).
10. Xu, H. *et al.* Electroluminescence from europium(III) complexes. *Coord Chem Rev* **293–294**, 228–249 (2015).
11. Cuttell, D. G. *et al.* Simple Cu(I) Complexes with Unprecedented Excited-State Lifetimes. *J Am Chem Soc* **124**, 6–7 (2002).
12. Leitl, M. J. *et al.* Phosphorescence versus Thermally Activated Delayed Fluorescence. Controlling Singlet–Triplet Splitting in Brightly Emitting and Sublimable Cu(I) Compounds. *J Am Chem Soc* **136**, 16032–16038 (2014).
13. Deaton, J. C. *et al.* [PNP-Cu]E-Type Delayed Fluorescence of a Phosphine-Supported Cu₂(μ-NAr₂)₂ Diamond Core: Harvesting Singlet and Triplet Excitons in OLEDs. *J Am Chem Soc* **132**, 9499–9508 (2010).
14. Hashimoto, M. *et al.* Highly efficient green organic light-emitting diodes containing luminescent three-coordinate copper(I) complexes. *J Am Chem Soc* **133**, 10348–10351 (2011).
15. Peng, Q. M. *et al.* Evidence of the Reverse Intersystem Crossing in Intra-Molecular Charge-Transfer Fluorescence-Based Organic Light-Emitting Devices Through Magneto-Electroluminescence Measurements. *Adv Opt Mater* **1**, 362–366 (2013).
16. Milián-Medina, B. & Gierschner, J. Computational design of low singlet–triplet gap all-organic molecules for OLED application. *Org Electron* **13**, 985–991 (2012).
17. Huang, S. *et al.* Computational Prediction for Singlet- and Triplet-Transition Energies of Charge-Transfer Compounds. *J Chem Theory Comput* **9**, 3872–3877 (2013).
18. Zhang, T. *et al.* Efficient triplet application in exciplex delayed-fluorescence OLEDs using a reverse intersystem crossing mechanism based on a DeltaES-T of around zero. *ACS Appl Mater Interfaces* **6**, 11907–11914 (2014).
19. Chaudhuri, D. *et al.* Tuning the singlet–triplet gap in metal-free phosphorescent pi-conjugated polymers. *Angew Chem Int Ed* **49**, 7714–7717 (2010).
20. Hung, W. Y. *et al.* Highly efficient bilayer interface exciplex for yellow organic light-emitting diode. *ACS Appl Mater Interfaces* **5**, 6826–6831 (2013).
21. Goushi, K., Yoshida, K., Sato, K. & Adachi, C. Organic light-emitting diodes employing efficient reverse intersystem crossing for triplet-to-singlet state conversion. *Nat Photon* **6**, 253–258 (2012).
22. Ishimatsu, R. *et al.* Electrogenenerated Chemiluminescence of Donor–Acceptor Molecules with Thermally Activated Delayed Fluorescence. *Angew Chem Int Ed* **53**, 6993–6996 (2014).
23. Jankus, V., Chiang, C. J., Dias, F. & Monkman, A. P. Deep Blue Exciplex Organic Light-Emitting Diodes with Enhanced Efficiency: P-type or E-type Triplet Conversion to Singlet Excitons? *Adv Mater* **25**, 1455–1459 (2013).
24. Masui, K., Nakanotani, H. & Adachi, C. Analysis of exciton annihilation in high-efficiency sky-blue organic light-emitting diodes with thermally activated delayed fluorescence. *Org Electron* **14**, 2721–2726 (2013).
25. Partee, J. *et al.* Delayed Fluorescence and Triplet–Triplet Annihilation in p-Conjugated Polymers. *Phys Rev Lett* **82**, 3673–3676 (1998).
26. Zheng, C.-J. *et al.* Novel Efficient Blue Fluorophors with Small Singlet–Triplet Splitting: Hosts for Highly Efficient Fluorescence and Phosphorescence Hybrid WOLEDs with Simplified Structure. *Adv Mater* **25**, 2205–2211 (2013).
27. Han, C. *et al.* Highly Efficient Multifluorenyl Host Materials with Unsymmetrical Molecular Configurations and Localized Triplet States for Green and Red Phosphorescent Devices. *Adv Mater* **26**, 7070–7077 (2014).
28. Han, C. *et al.* Rationally Investigating the Influence of T1 Location on Electroluminescence Performance of Aryl Amine Modified Phosphine Oxide Materials. *Chem Eur J* **20**, 16350–16359 (2014).
29. Zhu, Z.-Q., Fleetham, T., Turner, E. & Li, J. Harvesting All Electrogenenerated Excitons through Metal Assisted Delayed Fluorescent Materials. *Adv Mater* **27**, 2533–2537 (2015).
30. Cho, Y. J., Yook, K. S. & Lee, J. Y. High Efficiency in a Solution-Processed Thermally Activated Delayed-Fluorescence Device Using a Delayed-Fluorescence Emitting Material with Improved Solubility. *Adv Mater* **26**, 6642–6646 (2014).
31. Chen, X.-L. *et al.* Highly efficient cuprous complexes with thermally activated delayed fluorescence and simplified solution process OLEDs using the ligand as host. *J Mater Chem C* **3**, 1187–1195 (2015).
32. Tanaka, H., Shizu, K., Nakanotani, H. & Adachi, C. Twisted Intramolecular Charge Transfer State for Long-Wavelength Thermally Activated Delayed Fluorescence. *Chem Mater* **25**, 3766–3771 (2013).
33. Voyniuk, D. *et al.* Highly Efficient Blue Organic Light-Emitting Diodes Based on Intermolecular Triplet–Singlet Energy Transfer. *J Phys Chem C* **117**, 22538–22544 (2013).
34. Cho, Y. J., Yook, K. S. & Lee, J. Y. A universal host material for high external quantum efficiency close to 25% and long lifetime in green fluorescent and phosphorescent OLEDs. *Adv Mater* **26**, 4050–4055 (2014).
35. Wang, H. *et al.* Novel Thermally Activated Delayed Fluorescence Materials–Thioxanthone Derivatives and Their Applications for Highly Efficient OLEDs. *Adv Mater* **26**, 5198–5204 (2014).
36. Zhang, Q. *et al.* Design of efficient thermally activated delayed fluorescence materials for pure blue organic light emitting diodes. *J Am Chem Soc* **134**, 14706–14709 (2012).
37. Zhang, Q. *et al.* Efficient blue organic light-emitting diodes employing thermally activated delayed fluorescence. *Nat Photon* **8**, 326–332 (2014).
38. Adachi, C. *et al.* [CBP for Blue] Endothermic energy transfer: A mechanism for generating very efficient high-energy phosphorescent emission in organic materials. *Appl Phys Lett* **79**, 2082–2084 (2001).
39. Murawski, C., Leo, K. & Gather, M. C. Efficiency Roll-Off in Organic Light-Emitting Diodes. *Adv Mater* **25**, 6801–6827 (2013).
40. Kim, B. S. & Lee, J. Y. Engineering of Mixed Host for High External Quantum Efficiency above 25% in Green Thermally Activated Delayed Fluorescence Device. *Adv Funct Mater* **24**, 3970–3977 (2014).
41. Im, Y. & Lee, J. Y. Above 20% External Quantum Efficiency in Thermally Activated Delayed Fluorescence Device Using Furodipyridine-Type Host Materials. *Chem Mater* **26**, 1413–1419 (2014).
42. Ishimatsu, R. *et al.* Solvent effect on thermally activated delayed fluorescence by 1,2,3,5-tetrakis(carbazol-9-yl)-4,6-dicyanobenzene. *J Phys Chem A* **117**, 5607–5612 (2013).
43. Sasabe, H. *et al.* Influence of Substituted Pyridine Rings on Physical Properties and Electron Mobilities of 2-Methylpyrimidine Skeleton-Based Electron Transporters. *Adv Funct Mater* **21**, 336–342 (2011).
44. Su, S. J. *et al.* Structure-Property Relationship of Pyridine-Containing Triphenyl Benzene Electron-Transport Materials for Highly Efficient Blue Phosphorescent OLEDs. *Adv Funct Mater* **19**, 1260–1267 (2009).
45. Ye, H. *et al.* Pyridine-Containing Electron-Transport Materials for Highly Efficient Blue Phosphorescent OLEDs with Ultralow Operating Voltage and Reduced Efficiency Roll-Off. *Adv Funct Mater* **24**, 3268–3275 (2014).
46. Yook, K. S., Jang, S. E., Jeon, S. O. & Lee, J. Y. Fabrication and Efficiency Improvement of Soluble Blue Phosphorescent Organic Light-Emitting Diodes Using a Multilayer Structure Based on an Alcohol-Soluble Blue Phosphorescent Emitting Layer. *Adv Mater* **22**, 4479–4483 (2010).
47. Jeon, S. O., Jang, S. E., Son, H. S. & Lee, J. Y. External Quantum Efficiency Above 20% in Deep Blue Phosphorescent Organic Light-Emitting Diodes. *Adv Mater* **23**, 1436–1441 (2011).

48. Zhang, Q. *et al.* Triplet Exciton Confinement in Green Organic Light-Emitting Diodes Containing Luminescent Charge-Transfer Cu(I) Complexes. *Adv Funct Mater* **22**, 2327–2336 (2012).
49. Gong, S. *et al.* High-Power-Efficiency Blue Electrophosphorescence Enabled by the Synergistic Combination of Phosphine-Oxide-Based Host and Electron-Transporting Materials. *Chem Mater* **26**, 1463–1470 (2014).
50. Lee, J.-H. *et al.* An Exciplex Forming Host for Highly Efficient Blue Organic Light Emitting Diodes with Low Driving Voltage. *Adv Funct Mater* **25**, 361–366 (2015).
51. Jia, J. *et al.* Triazine-phosphine oxide electron transporter for ultralow-voltage-driven sky blue PHOLEDs. *J Mater Chem C* **3**, 4890–4902 (2015).
52. Kang, N. S. *et al.* Correlation of photoluminescent quantum efficiency and device characteristics for the soluble electrophosphorescent light emitter with interfacial layers. *J Appl Phys* **104**, 024511 (2008).
53. Chen, Z. *et al.* Enhanced green electrophosphorescence by using polyfluorene host via interfacial energy transfer from polyvinylcarbazole. *Org Electron* **9**, 1002–1009 (2008).
54. Wang, Z. B. *et al.* Controlling carrier accumulation and exciton formation in organic light emitting diodes. *Appl Phys Lett* **96**, 043303 (2010).
55. Nowy, S. *et al.* Impedance spectroscopy as a probe for the degradation of organic light-emitting diodes. *J Appl Phys* **107**, 054501 (2010).
56. Han, T.-H. *et al.* Molecularly Controlled Interfacial Layer Strategy Toward Highly Efficient Simple-Structured Organic Light-Emitting Diodes. *Adv Mater* **24**, 1487–1493 (2012).
57. Kan, W. *et al.* Phosphine oxide-jointed electron transporters for the reduction of interfacial quenching in highly efficient blue PHOLEDs. *J Mater Chem C* **3**, 5430–5439 (2015).
58. Becke, A. D. Density-functional thermochemistry. III. The role of exact exchange. *J Chem Phys* **98**, 5648–5652 (1993).
59. Lee, C., Yang, W. & Parr, R. G. Development of the Colle-Salvetti correlation-energy formula into a functional of the electron density. *Phys Rev B* **37**, 785–789 (1988).
60. de Leeuw, D. M., Simenon, M. M. J., Brown, A. R. & Einerhand, R. E. F. Stability of n-type doped conducting polymers and consequences for polymeric microelectronic devices. *Synthet Met* **87**, 53–59 (1997).
61. Wang, Z. B. *et al.* Carrier mobility of organic semiconductors based on current-voltage characteristics. *J Appl Phys* **107**, 034506 (2010).

Acknowledgements

This project was financially supported by NSFC (61176020 and 51373050), New Century Excellent Talents Supporting Program of Ministry of Education (NCET-12-0706), Program for Innovative Research Team in University (Ministry of Education) (IRT-1237), Science and Technology Bureau of Heilongjiang Province (ZD201402 and JC2015002), Education Bureau of Heilongjiang Province (2014CJHB005) and the Fok Ying-Tong Education Foundation for Young Teachers in the Higher Education Institutions of China (141012).

Author Contributions

C.D. and C.F. contributed equally to this work. H.X. conceived and designed the experiments. C.D. and F.H. fabricated and measured the devices. C.F. and C.D. performed the synthesis and physical analysis. W.H. and Y.W. analyzed the data. H.X. and C.D. wrote the paper. All authors commented on the manuscript.

Additional Information

Supplementary information accompanies this paper at <http://www.nature.com/srep>

Competing financial interests: The authors declare no competing financial interests.

How to cite this article: Duan, C. *et al.* Optimizing the Intralayer and Interlayer Compatibility for High-Efficiency Blue Thermally Activated Delayed Fluorescence Diodes. *Sci. Rep.* **6**, 19904; doi: 10.1038/srep19904 (2016).



This work is licensed under a Creative Commons Attribution 4.0 International License. The images or other third party material in this article are included in the article's Creative Commons license, unless indicated otherwise in the credit line; if the material is not included under the Creative Commons license, users will need to obtain permission from the license holder to reproduce the material. To view a copy of this license, visit <http://creativecommons.org/licenses/by/4.0/>